**Mathematical Biology**

Mark T. Stacey · Kristina S. Mead · Mimi A. R. Koehl

# Molecule capture by olfactory antennules: Mantis shrimp

**Abstract.** A critical step in the process of olfaction is the movement of odorant molecules from the environment to the surface of a chemosensory structure. Many marine crustaceans capture odorant molecules with arrays of chemosensory sensilla (aesthetascs) on antennules that they flick through the water. We developed a model to calculate molecule flux to the surfaces of aesthetascs in order to study how the size, aesthetasc spacing, and flick kinematics of olfactory antennules affect their performance in capturing molecules from the surrounding water. Since the three-dimensional geometry of an aesthetasc-bearing antennule is complex, dynamically-scaled physical models can often provide an efficient method of determining the fluid velocity field through the array. Here we present a method to optimize the incorporation of such measured velocity vector fields into a numerical simulation of the advection and diffusion of odorants to aesthetasc surfaces. Furthermore, unlike earlier models of odorant interception by antennae, our model incorporates odorant concentration distributions that have been measured in turbulent ambient flows. By applying our model to the example of the olfactory antennules of mantis shrimp, we learned that flicking velocity can have profound effects on odorant flux to the aesthetascs if they operate in the speed range in which the leakiness of the gaps between the aesthetascs to fluid movement is sensitive to velocity. This sensitivity creates an asymmetry in molecule fluxes between outstroke and return stroke, which results in an antennule taking discrete samples in space and time, i.e. "sniffing". As stomatopods grow and their aesthetasc Reynolds number increases, the aesthetasc arrangement on the antennule changes in a way that maintains these asymmetries in leakiness and molecule flux between the outstroke and return stroke, allowing the individual to continue to take discrete samples as it develops.

## 1. Introduction

Many marine animals use water-borne chemical cues in ecologically-important activities such as locating food, selecting habitats, detecting predators or competitors, and communicating with conspecifics [14], [15], [1], [36], [78], [11], [74], [73], [77], [4], [7], [75], [76]. A critical step in the process of olfaction is the arrival of

M.T. Stacey: Department of Civil and Environmental Engineering, 509 Davis Hall, University of California, Berkeley, Berkeley, CA 94720-1710, USA.
e-mail: `mstacey@socrates.berkeley.edu`

K.S. Mead, M.A.R. Koehl: Department of Integrative Biology, 3060 VLSB, University of California, Berkeley, Berkeley, CA 94720-3140, USA

chemical signals from the environment to the surface of a chemosensory structure. From a hydrodynamic standpoint, this process can be broken up into two regimes based on scale: 1) large-scale turbulent water flow transports the odorant from the source to the immediate vicinity of the sensor; and 2) small-scale viscous flow and molecular diffusion transport the odorant to the surface of the sensor [22], [44], [52], [68], [69], [28]. In this study, we will take the structure imposed by the large-scale turbulent flow as a starting point for our analysis, while we focus on the small-scale advection and molecular diffusion of an odorant filament through an array of olfactory hairs to define the capture of odorant by chemosensory sensilla.

Odorant concentration distributions are patchy in turbulent wind [25], [63] and water currents [6], [59], [79], [5], [76]. Recent studies using planar laser-induced fluorescence to visualize the spatial distribution of concentration in plumes in water revealed fine filaments (< 1 mm thick) of high concentration interspersed with layers of clean water [20], [72]. Our purpose here is to explore how the small-scale viscous flow and molecular diffusion near olfactory organs transports odorants in such filamentous plumes to sensor surfaces. The olfactory organs on which we focus are the antennules of crustaceans.

### 1.1. Crustacean olfactory antennules

Many marine crustaceans (e.g. a variety of malacostracans such as stomatopods, lobsters, and crabs) capture odorant molecules with their antennules, which bear arrays of hair-like structures called "aesthetascs" that contain chemosensory neurons [40], [37].

A variety of crustaceans flick their olfactory antennules. It has been suggested [31], [3], [70], [34] that densely-packed aesthetascs on the antennules of various crustaceans inhibit flow and odor access, as corroborated by microelectrode measurements of reduced molecule fluxes within aesthetasc tufts on lobster lateral antennules, but not near smooth medial antennules [58], [60]. Antennule flicking has been described as a mechanism of reducing boundary layer thickness, thereby increasing access of odors to receptor cells [66], [3], [70], [23], [33], [38], [52] and synchronizing the arrival of signal along the antennule [32]. Several lines of evidence are consistent with this idea. Flow pulses onto the aesthetascs of antennule preparations to mimic flicking increased penetration of molecules into tufts of aesthetascs [58], [60], and enhanced the response of lobster olfactory receptor neurons to changes in odor concentration [66].

These experiments with isolated antennule preparations [58], [60], [66] were done before information was available about the kinematics of [54], [34] and small-scale flow fields through [48], [47], [55], hair arrays on antennules, or about the spatio-temporal distribution of odorant concentrations in aquatic turbulent plumes [20], [72] (Koehl, Koseff, Crimaldi, McCay, Cooper, Wiley, and Moore, in prep.). Furthermore, they did not address a critical step in odorant capture: molecule flux to aesthetasc surfaces. In the present study we develop a model that can incorporate data, both about flow fields through aesthetasc arrays and about odorant concentration distributions in plumes, to explore how antennule morphology and kinematics affect molecule flux to aesthetasc surfaces.

*1.2. Fluid motion and molecule transport near hairs*

The Reynolds number ($Re = \frac{LU}{\nu}$, where $L$ is a linear dimension, $U$ is velocity, and $\nu$, is the kinematic viscosity of the fluid) represents the relative importance of inertial to viscous forces for a flow situation. The Reynolds numbers of olfactory sensilla (or aesthetascs) on a variety of arthropods are low: $10^{-4}$ to 10, calculated using the sensillum diameter for $L$ [51], [54], [48], [47]. Although inertial effects cannot be ignored at the upper end of this Re range, the viscous flow near sensory aesthetascs is laminar (i.e. fluid motion is smooth and orderly, with no random fluctuations in velocity; [39], [71]). When a sensillum moves through a viscous fluid, the layer of fluid in contact with its surface does not slip relative to the surface and a velocity gradient develops in the fluid around the sensillum. At low $Re$, at which olfactory sensilla operate, such laminar boundary layers are thick relative to the dimensions of a sensillum [17]. There is no turbulent mixing in a laminar boundary layer, hence molecular diffusion is the mechanism that moves odorants across streamlines towards or away from the surface of a sensillum.

While several authors have suggested that the time course of the initial phases of neural responses to odorants might be determined by the transport of molecules to the receptor [29], [22], [65], [30], [58], [61], others have argued that molecular diffusion is not a limiting barrier to access to odor molecules [28], [53], [13]. This issue has been addressed by calculations of the diffusion of odor molecules to the surfaces of receptors [2], [9], [64], [22], [10], [28], [30], [42]. However, in spite of the importance of small-scale fluid flow to this process, information about velocity profiles near actual biological geometries of sensillum arrays was not available at the time that these models were developed. Therefore, various flow fields have been assumed in these models that are not necessarily appropriate, hence the applicability of their conclusions to specific organisms is not yet clear. Due to recent advances in particle image velocimetry [19], we have been able to measure flow fields around dynamically scaled models of real olfactory appendages. We are therefore able to use realistic flow fields as inputs for our advection-diffusion model of an odor filament moving through an array of aesthetascs.

Early calculations of the diffusion of odor molecules to sensors approximated the sensillum as a single infinitely long cylinder [2], [64]. More recent studies have focused on the effects that cylinder arrays of finite width have on the fluid flow between neighboring cylinders [18], [51], [44], [46]. If the boundary layers of fluid moving along with the sensilla in an array are thick relative to the gaps between the sensilla, then little fluid may leak through the array. Mathematical and physical modeling of the fluid dynamics of arrays of sensilla has revealed a transition in the performance of such structures between aesthetasc Reynolds number ($Re$) of $10^{-2}$, where they resist fluid motion through the array and function like paddles, and $Re$ of 1, where they are quite leaky to fluid flow and function like sieves (unless the sensilla are very close together) [17], [18], [43], [44], [45], [46], [48], [47], [51]. The $Re$ range in which the transition in leakiness occurs depends on the geometry of the appendage: the wider the gap between neighboring sensilla relative to sensillum diameter, the lower the $Re$ at which this transition between paddle-like and sieve-like function occurs. The chemosensory sensilla on a variety of olfactory

antennae operate in a range of *Re* and sensillum spacings in which changes in velocity and changes in sensillum spacing can have profound effects on the flow near the sensilla [45], [48], [47], [54]; [55]; [52].

### 1.3. Stomatopods as a model system

We are using stomatopod antennules as a model system for studying the effects of flow near chemosensory aesthetascs on their performance in capturing molecules. Stomatopods ("mantis shrimp"), which are aggressive predatory crustaceans, use olfactory information during critical biological activities such as locating food, communicating with potential mates, and mediating aggressive interactions with conspecifics [14], [16]. The arrangement of aesthetascs on stomatopod antennules is simple (Figure 1) [54], thus physical and mathematical modeling of water flow near and molecule diffusion to aesthetascs is more tractable for stomatopods than for the more complex antennules of lobsters or crabs. Furthermore, stomatopods provide a system in which the effects of body size (and thus, aesthetasc *Re*, which uses the aesthetasc diameter as the length scale) on molecule capture can be investigated since juveniles are only a few millimeters long but grow into adults many centimeters in body length.

In this study, we concentrate on the subtidal tropical Hawaiian stomatopod, *Gonodactylaceous mutatus*. Morphometric and kinematic analyses of the antennules of this species have been conducted for juvenile and adult animals representing a range of body sizes [54]. These stomatopods flick their olfactory antennules laterally at aesthetasc *Re* of 0.2 for small juveniles (8 mm in body length) to 1.8 for adults (52 mm in body length). The animals then return the antennules medially at half the speed of the outstroke. These data have been used to design dynamically-scaled physical models of the antennules of juvenile and adult *G. mutatus*, and particle image velocimetry [19] was used to measure the velocity fields around the aesthetascs of the models operating at various *Re* [55]. These experiments showed that the antennules of *G. mutatus* operate in a range of *Re* in which the leakiness to water flow of the array of aesthetascs during the rapid outstroke was much greater than during the slower medial return stroke.

### 1.4. Neurobiology of aesthetascs

The aesthetascs on stomatopod antennules are hair-like structures composed of a thin cuticle surrounding many olfactory receptor neurons. Transmission electron microscopy (TEM) measurements show that the cuticle is only 0.6 to 1 mm thick, and dye studies indicate that the cuticle is permeable to small molecules (Mead and Weatherby, submitted). TEM has also revealed that the distal two thirds of the aesthetasc is filled with the highly branched outer dendritic segments of the sensory cells. Olfaction occurs when odor molecules are carried by advection of ambient water to the vicinity of an aesthetasc, arrive at the aesthetasc surface via molecular diffusion, diffuse through the cuticle into the lumen of the aesthetasc, and bind to receptors on an outer dendritic segment of an olfactory neuron. When enough odor molecules bind to the receptors on a neuron, the neuron depolarizes ("spikes") and

the signal is transmitted to the olfactory lobe of the brain, where it is processed [56], [57], [67]. In this study, we are focusing on the flux of molecules to the surface of the aesthetascs due to the physical processes of advection and diffusion.

Neurobiological studies indicate which aspects of odor molecule flux are important to crustacean olfactory neuron firing. Experiments delivering precise pulses of known concentrations of odors to exposed axons of olfactory neurons in lobster antennules demonstrate that single neurons produce more spikes when odor concentration is increased, and that the delay between odor delivery and the first spike is decreased at higher odor concentration [35]. Cells also increase the number of spikes produced when the duration of the applied pulse (pulse peak width) is increased [35]. Moore's [62] mathematical model of adaptation and de-adaptation in olfactory receptor neurons suggests that single cells can distinguish between different rates of increasing odor concentration (onset slope). Cells that adapt quickly (i.e. that change the response threshold of the cell to the level of the stimulus) only respond to pulses with steep slopes. In contrast, slowly adapting cells respond to odor pulses with shallow onset slopes as well as to those with steep onset slopes [62]. Hence, the responses of a population of cells should distinguish between a variety of pulse slopes. We suspect that stomatopod olfactory receptor cells, like those of lobsters [35] must interact with a particular number of molecules within a period of time in order to fire (analogous to the visual system, in which photoreceptor cells respond to light only if a certain threshold amount of energy is received within a critical time period [8], [41]). Therefore, the aspects of molecule flux at the aesthetasc surface on which we will focus are: maximum molecule flux, maximum onset slope (i.e., maximum rate of increase of molecule flux), and total number of molecules detected in a pulse of odor.

## 1.5. Objectives

Our primary objective is to establish a method that will enable us to calculate molecular fluxes at the sensillar surfaces of olfactory antennae. Whereas previous modeling efforts have relied largely upon idealizations, such as flow around individual cylinders [2], [64], or examined the transport of rare molecules [52], we will simulate the advection and diffusion of a filament of odorant molecules (consistent with observations in a marine boundary layer, [20]) through an array of sensilla. As noted by Murray [64], an array of sensilla is expected to modify the flow field and perturb the results obtained when considering isolated cylinders. In order to determine the flow field through the array, we will incorporate empirically-determined flow fields [55], but require that the flow field used for the simulation be consistent with the continuity equation – providing a strict constraint on the optimization of the flow field. Once the flow field is so defined, we will simulate the advection and diffusion of odorant through the array and define the flux of odorant to the sensillar surfaces. Using this model, the specific questions that we address are:

1) What effect does the difference in antennule velocity during the outstroke versus the slower return stroke have on molecule capture?
2) What effects do the ontogenetic changes in antennule size, morphology, and kinematics have on molecule capture?

3) Do the proximal and distal ends of an aesthetasc experience different fluxes of molecules?
4) Does the position of an aesthetasc within a row of aesthetascs affect the flux of molecules to its surface?

## 2. Methods

The primary objective of the current study is to develop a model of odorant fluxes to sensiliar surfaces in an array of aethetascs. Towards that end, we apply a numerical model of odorant advection and diffusion, which will resolve the time variability of the flux of odorant molecules to the surface of the sensilla. This numerical model requires an estimate of the flow-field through the array of sensilla, which will advect the odorant while molecular processes act to diffuse the odorant across streamlines. The numerical model will be described in section 2.2, but first we discuss the analysis required to define an appropriate advective field (section 2.1).

### 2.1. Flow field analysis

In order to resolve the advection of odorant molecules, we require an estimate of the water velocity fields relative to the aesthetascs during the flick outstroke and during the return stroke. For our discussion here, stomatopod antennules – of both adult and juvenile morphology – are analyzed, both at the natural aesthetasc Reynolds number as well as at other Reynolds numbers. The orientation of the aesthetascs with respect to the fluid motion during a flick of the antennule is diagrammed in Figure 1d.

As an individual flicks its antennule, the ambient water is forced into and around the aesthetasc array on the antennule. In the reference frame of the antennule, however, it appears that the ambient fluid is flowing into the array with a velocity set by the speed of the flick. At its simplest, therefore, the flow we are examining is uniform flow that encounters an array of cylinders (the antennule and aesthetascs). In order to define the flow through an array of aesthetascs, we rely on actual measurements of flow through stomatopod aesthetascs, made with dynamically-scaled laboratory models. The measurements, however, may not be consistent with the continuity equation, which is required for advection-diffusion modeling as we will undertake. As a result, we will need to define an optimal flow field, which minimizes the error defined by the observations while obeying the continuity equation (defining a strict constraint on the flow field). In the next section, we discuss briefly the measurements of flow through the array of aesthetascs. Then, we present the analysis necessary to provide a velocity field suitable for the numerical simulations.

### 2.1.1. Flow through the array of aesthetascs

The flow around the antennule, which is simply flow around a cylinder, is perturbed by the presence of the array of aesthetascs, which are oriented at an oblique angle to the antennule (approximately 50 degrees) (Figure 1a, 1c). In our analysis, we consider the plane normal to the aesthetascs (Figure 1c). The flow entering the
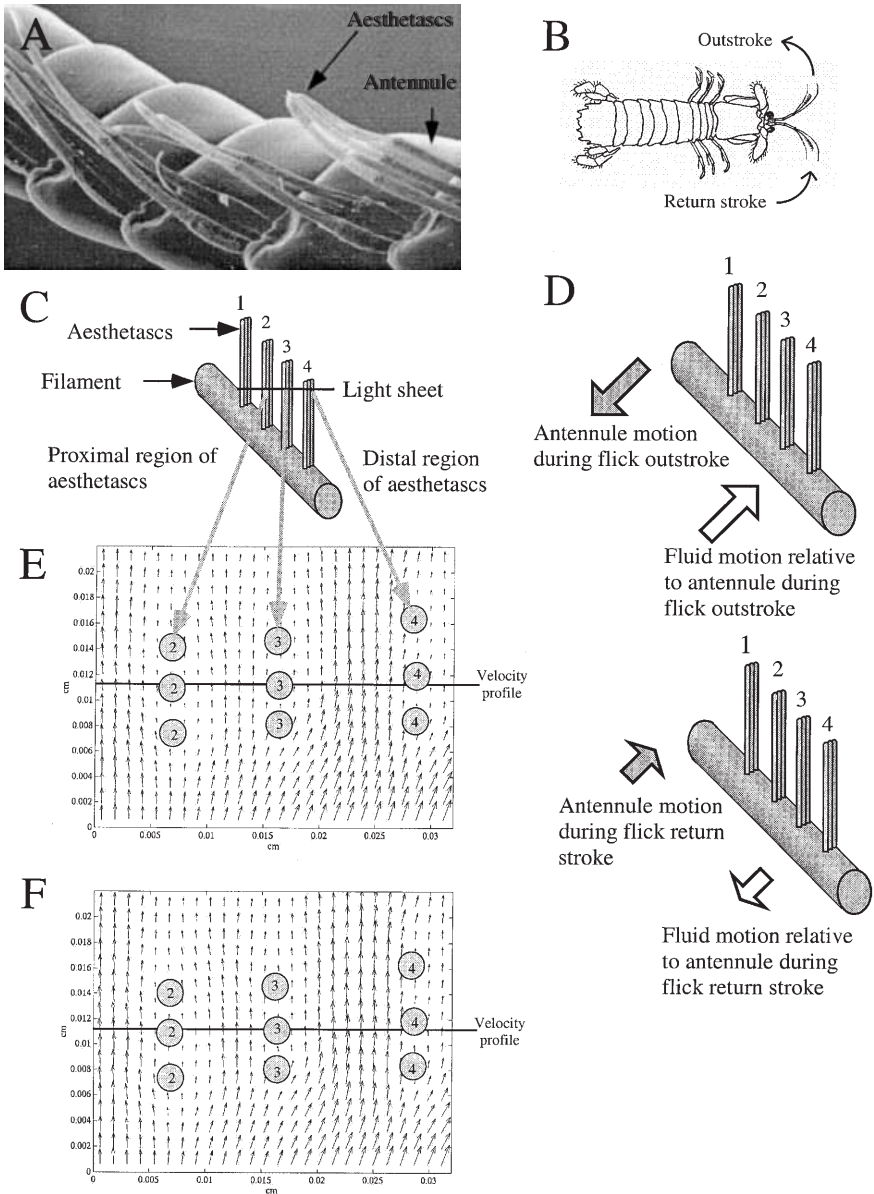
**Fig. 1.** Stomatopod model geometry. (A) Image of stomatopod antennule with aesthetascs. (B) Dorsal view of stomatopod showing flick outstroke and return stroke. (C) Cartoon of the dynamically scaled model of part of an adult stomatopod antennule showing four rows of three aesthetascs. (D) Antennule and fluid motion during the outstroke and return stroke of an olfactory flick. Filled arrows indicate antennule motion; light arrows show fluid motion. Arrow length corresponds to speed. (E) Top view of physical model as it intersects the light sheet. Circles represent top views of aesthetascs; the number indicates the aesthetasc row. Arrows show the magnitude and direction of the fluid motion relative to the model at the level of the light sheet. (F) Raw velocity field (PIV data; see methods); (F) Velocity field corrected so that it obeys the continuity equation (see method).

aesthetasc array contains shear resulting from the flow field set up around the an-
tennule, so the shear in the plane normal to the aesthetascs is set by the flow around
the antennule and the angle the aesthetascs make with the antennule.

In our analysis, we use PIV measurements of fluid velocities relative to the
aesthetascs in a plane normal to the aesthetascs but oblique to the antennule (Fig-
ure 1c) (means of 10 experiments for each case in Table 1, [55]). An example of
such a velocity field is shown in Figure 1e. We are able to resolve the flows around
the aesthetascs in a plane normal to them, but we are not able to resolve the third
dimension of the flow. These measured velocities are entirely empirical and may
or may not be consistent with the governing equations, particularly the continuity
equation (conservation of mass). Therefore, these planar data must be analyzed
to ensure mass conservation and to determine whether flows out of the plane of
measurement are small.

### 2.1.2. Decomposition of measured velocity fields

The velocity fields defined by the PIV technique provide us with a starting point for
developing a flow field for use with the numerical model. We would like to use these
velocity fields to drive the advective component of the advection-diffusion model
(discussed below, section 2.2). For the application to mass transport, however, the
planar velocity field *must* obey the two-dimensional continuity equation (note that
boldface denotes vector quantities):

$$\nabla \cdot \mathbf{U} = \frac{\partial u}{\partial x} + \frac{\partial v}{\partial y} = 0 \tag{1}$$

where we define the velocity in the x-direction to be $u$ and in the y-direction
to by $v$ ($\mathbf{U} = (u, v)$). Because the velocity fields described above are based on
measurements, they may not be consistent with the continuity equation. Therefore,
we must decompose the observed velocity field into a component which obeys the
continuity equation ($\mathbf{U_{nd}}$, the non-divergent flow field) and a component which
does not ($\mathbf{U_d}$, the divergent flow field). Thus, we separate the observed velocity
field, $\mathbf{U_{obs}}$, into two parts:

$$\mathbf{U_{obs}} = \mathbf{U_{nd}} + \mathbf{U_d} \tag{2}$$

where

$$\nabla \cdot \mathbf{U_{nd}} = 0 \tag{3}$$

$\mathbf{U_{nd}}$ obeys the continuity equation and is the portion of the velocity field that we
use to define the transport of odorant.

In three dimensions, the continuity equation includes the gradient of the vertical
velocity:

$$\frac{\partial u}{\partial x} + \frac{\partial v}{\partial y} + \frac{\partial w}{\partial z} = 0 \tag{4}$$

If the two-dimensional continuity equation (equation 1) is violated by the measured
velocities, it indicates that the third gradient is not zero (that is, $\frac{\partial w}{\partial z} \neq 0$). There-
fore, the degree to which the two-dimensional continuity equation is violated by
the observations is a measure of the importance of the third dimension. The result

of this decomposition for every velocity field considered was quite similar to the original flow field (discussed further below), indicating that the flow through the aesthetascs is nearly planar, and is in the plane of the measurements.

Separation of the velocity field into divergent and non-divergent components is based on the Helmholtz decomposition [26]. We define a velocity potential, $\phi$, such that:

$$\nabla\phi = \mathbf{U_d} \qquad (5)$$

Because we require that $\nabla \cdot \mathbf{U_{nd}} = 0$, we know that:

$$\nabla \cdot \mathbf{U_d} = \nabla^2\phi = \nabla \cdot \mathbf{U_{obs}} \qquad (6)$$

which defines an equation for $\phi$ based on the observed velocities. Equation (6) can be solved directly using a finite difference approximation for the derivatives. This equation was solved using a central-difference for all derivatives, which results in a matrix equation for $\phi$ which we solve through direct matrix inversion.

Once $\phi$ is defined, we calculate $\mathbf{U_d}$ and subtract it from the original data set to define $\mathbf{U_{nd}}$:

$$\mathbf{U_{nd}} = \mathbf{U_{obs}} - \nabla\phi \qquad (7)$$

which satisfies the continuity equation. While the resulting velocity fields are quite similar to the observations, they may not be the optimal choice of flow fields, which is the subject of the next section.

### 2.1.3. Optimization of modeled velocity fields

The divergence-free flow field that results from the analysis described in the previous section ($\mathbf{U_{nd}}$) provides us with an initial guess of a velocity field which will be similar to the observations and is consistent with the two-dimensional continuity equation. This flow field, however, may not be the *optimal* one; that is, the one that minimizes the difference between the modeled and observed flow fields while still obeying continuity. We now discuss the optimization required to define the optimal flow field, which we will define to be $\mathbf{U_m}$ (the velocity field to be used in the model).

As mentioned above, the two-dimensional continuity equation (1) provides a strong constraint on this minimization. A non-divergent flow field (i.e., one that obeys equation(1)) can always be written in terms of a streamfunction, $\Psi$:

$$\mathbf{U} = (-\frac{\partial \Psi}{\partial y}, \frac{\partial \Psi}{\partial x}) \qquad (8)$$

which ensures that (1) is satisfied by $\mathbf{U}$.

We make use of this relationship to define our modeled velocity field as:

$$\mathbf{U_m} = \mathbf{U_{nd}} + \mathbf{U'} \qquad (9)$$

where $\mathbf{U_{nd}}$ is the result of the decomposition described in the previous section and:

$$\mathbf{U'} = (-\frac{\partial \Psi'}{\partial y}, \frac{\partial \Psi'}{\partial x}) \qquad (10)$$

and the continuity condition is automatically enforced. The optimization now simply needs to define the best choice of $\Psi'$ in view of the observations. The objective of the minimization will be the mean-square-error, where the error is defined as:

$$\mathbf{e} = \mathbf{U_{obs}} - \mathbf{U_m} = \mathbf{U_{obs}} - \mathbf{U_{nd}} - (-\frac{\partial \Psi'}{\partial y}, \frac{\partial \Psi'}{\partial x}) \tag{11}$$

To define the mean-square-error, we integrate the magnitude squared of $\mathbf{e}$ over the domain to define the function to minimize, $E$. Defining $\mathbf{d}$ to be the difference between the observations and our initial guess at the velocity field (i.e., $\mathbf{d} = (d_1, d_2) = \mathbf{U_{obs}} - \mathbf{U_{nd}}$), we can write $E$ as:

$$E = \int_0^{L_x} \int_0^{L_y} [d_1^2 + 2d_1 \frac{\partial \Psi'}{\partial y} + (\frac{\partial \Psi'}{\partial y})^2 + d_2^2 - 2d_2 \frac{\partial \Psi'}{\partial x} + (\frac{\partial \Psi'}{\partial x})^2] dy dx \tag{12}$$

We now choose the scalar function $\Psi'$ which minimizes $E$.

In order to perform this minimization, we decompose our unknown function into its two-dimensional Fourier components:

$$\Psi' = \sum_{m,n} A_{mn} \sin(\frac{m\pi x}{L_x}) \sin(\frac{n\pi y}{L_y}) \tag{13}$$

which forces our streamfunction to be zero at all four boundaries (which does not constrain our solution in any way, since the velocity field depends only on the gradient of the streamfunction). Substituting this expression into equation (12), the condition for an extremum of the error:

$$\frac{\partial E}{\partial A_{mn}} = 0 \tag{14}$$

defines a series of equations for each coefficient, $A_{mn}$. The solution of these equations is given by:

$$A_{mn} = \frac{8\pi L_x L_y}{n^2 \pi^2 L_x^2 + m^2 \pi^2 L_y^2} (I_2 - I_1) \tag{15}$$

where

$$I_2 = m \int \int d_2 \cos(\frac{m\pi x}{L_x}) \sin(\frac{n\pi y}{L_y}) dy dx \; ; \tag{16}$$

$$I_1 = n \int \int d_1 \sin(\frac{m\pi x}{L_x}) \cos(\frac{n\pi y}{L_y}) dy dx \tag{17}$$

and where the double integrals are over the domain (as in equation (12)). We further note that the second derivatives of the error are given by:

$$\frac{\partial^2 E}{\partial A_{mn}^2} = \frac{1}{4} (n^2 \pi^2 L_x/L_y + m^2 \pi^2 L_y/L_x) > 0 \tag{18}$$

thus ensuring that the extremum defined by equation (15) is a minimum of the error function.

To define our model velocity fields, we subsitute (15), (16) and (17) for $A_{mn}$ in equation (13), and use the resulting streamfunction, $\Psi'$, to define the model flow field using (9) and (10). Comparison between the original data ($\mathbf{U_{obs}}$, Figure 1e) and the analyzed data ($\mathbf{U_m}$, Figure 1f) indicates that the measurements are nearly consistent with continuity and that only minor alterations to the velocity field are needed. This is true for all the velocity fields used in this study. These two-dimensional velocity fields provide the basis for the numerical simulations outlined below.

### 2.2. Numerical calculation of odor transport

The goal of this model development is to simulate the flux of odorant molecules to individual aesthetascs. In previous models of molecule capture, odorant molecules were tracked individually (through random walk models, for example [52]). For a steady source of odorant (such as a food source or a mate) in a turbulent marine boundary layer, the odorant plume is strained into small filaments [20], with the dimensions of the distribution defined by the background turbulence structures. In view of this, we would like to model the advection and diffusion of odorant using a concentration-based approach (i.e., a continuous distribution as opposed to individual particles), where we can examine the motion and deformation of a filament into and through an array of aesthetascs. In this section, we describe the numerical details of the advection-diffusion model.

The transport model solves the two-dimensional advection-diffusion equation. For a scalar, ($c$), in the absence of sources and sinks:

$$\frac{\partial c}{\partial t} + u_m \frac{\partial c}{\partial x} + v_m \frac{\partial c}{\partial y} = D(\frac{\partial^2 c}{\partial x^2} + \frac{\partial^2 c}{\partial y^2}) \tag{19}$$

where the velocity fields ($u_m(x, y)$ and $v_m(x, y)$) are as defined above by the optimization (figure 1f) and the molecular diffusion coefficient is a constant with a value of $D = 10^{-9}$ m$^2$/s for an amino acid in water [21].

The numerical method to solve this equation is a finite difference formulation on a staggered grid. The grid is shown in Figure 2, with the concentrations defined at the center of the cells and the velocities defined at the faces. The staggered grid allows advection to be discretized more accurately than for an unstaggered grid. On this grid, the diffusion terms are discretized with central differences [26]. At $c_{i,j}$, the diffusion in the x-direction is approximated as:

$$D \frac{\partial^2 c}{\partial x^2} = D \frac{c_{i+1,j} - 2c_{i,j} + c_{i-1,j}}{\Delta x^2} \tag{20}$$

The advective terms are discretized using the QUICK algorithm (Quadratic Upstream Interpolation for Convective Kinematics) [50]. For flow in the positive y-direction at a velocity, $v$, advection is approximated as:

$$v \frac{\partial c}{\partial y} = v_j \frac{1}{\Delta y} [\frac{1}{2}(c_j + c_{j+1}) - \frac{1}{8}(c_{j-1} - 2c_j + c_{j+1})$$
$$- \frac{1}{2}(c_{j-1} + c_j) + \frac{1}{8}(c_{j-2} - 2c_{j-1} + c_j)] \tag{21}$$
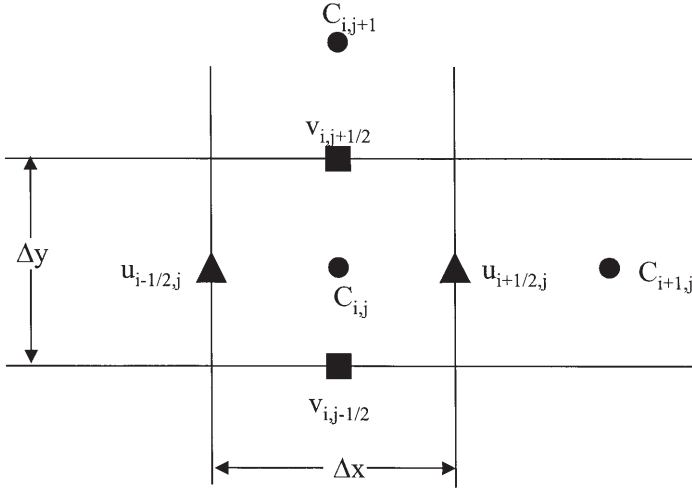
**Fig. 2.** Definition of grid for numercial simulations. Concentration is defined at center of grid cells ($C_{ij}$, e.g.), and velocity is defined on the faces of the cell. In the x-direction, the velocity is $u$, the grid has spacing $\Delta x$ with grid index $i$. In the y-direction (the primary flow direction), the velocity is $v$, the spacing is $\Delta y$ and the index is $j$.

The QUICK algorithm is second order accurate and has no artificial diffusion, so that the simulation accurately represents the molecular diffusion [50]. The temporal derivative is approximated using an explicit forward timestep, for which the QUICK formulation of advection forces a limit on the size of the timestep to ensure stability:

$$\Delta t < \frac{2D}{v^2} \tag{22}$$

The boundary conditions are free-flow through all open boundaries, so odorant can pass freely out of the domain (i.e., odorant molecules can be carried out of, but not into, the domain by the flowing water, and there is no diffusion of odorant molecules across the boundaries).

The initial condition for the concentration of odorant is a "filament" which is uniform in the cross-flow direction. In the flow direction, the filament has a Gaussian shape, with a width of approximately 1 mm to be consistent with measurements of concentrations in dye filaments encountering antennules on animals 1 meter downstream from an oozing dye source on the substratum of a flume (turbulent flow, 0.10 m/s) (Koehl, Koseff, Crimaldi, Cooper, McCay, Wiley and Moore, in prep.). The distance from the center of the filament to the leading aesthetascs is prescribed to be the same for all cases (0.5 mm). The peak concentration in the odor filament is set to 100 $\mu$moles/l $= 10^{-7} \frac{\text{moles}}{\text{cm}^3} = 6.022 * 10^{16} \frac{\text{molecules}}{\text{cm}^3}$, to match concentrations used in neurobiological experiments on crustacean olfactory antennules [35]. In order to compare the effect of kinematics of the outstroke versus the return stroke on molecule capture, we model the antennule during the return stroke as it encounters a filament identical to the one it encounters during

the outstroke, but approaching from the opposite side of the antennule (i.e. from the upstream side during the return stroke). In our return-stroke model, the antennule does not encounter an already-processed filament that had passed across the aesthetasc array during the outstroke.

An example of the advection and diffusion of the filament is shown in Figure 3. at four different times during the flick outstroke by an adult antennule. The initial condition is shown in Figure 3b and Figures 3c-e show the development at three later times. For reference, in Figure 3a the location of the filament of odorant relative to the aesthetascs is shown for each of the times in Figures 3b-e, with the odor filament advecting at the flick velocity (i.e., the flow in the absence of aesthetascs). For these calculations, we assume that the odorant molecules are removed from the water instantaneously when they contact the surface of an aesthetasc. For modeling purposes, this preserves a concentration of zero in the interior of each aesthetasc: we track the amount of odorant which is removed by the aesthetascs to know the number of odorant molecules per time arriving at a defined area of an aesthetasc to determine the flux of molecules captured.

The advection-diffusion model produces a timeseries of the molecule concentration at the aesthetasc surface. At each point in time, the molecule concentration, $C_{aes}$, is translated into a molecule flux (number of molecules per time per area) by multiplying by the grid spacing and dividing by the timestep and the circumference of the aesthetasc. That is, we define:

$$F_{aes} = 10^{-11} C_{aes} \frac{\Delta x \Delta y}{\Delta t (2\pi r)} \tag{23}$$

where $F_{aes}$ is the flux of molecules per millisecond (ms) and per square micron ($\mu$) of surface area of the aesthetasc (assuming a unit length in the along-aesthetasc direction); $\Delta t$ is the model time step, $\Delta x$ and $\Delta y$ are the grid spacings in each dimension, and $r$ is the radius of the aesthetasc. The scaling by $10^{-11}$ accounts for the change of units from centimeters to microns and seconds to milliseconds.

## 3. Results

The analysis of molecule capture by stomatopods includes several cases. First of all, the natural Reynolds numbers and morphologies for juvenile and adult individuals are considered, focusing on the upstream aesthetascs (see Figure 1d). Then, we analyze the effects of different Reynolds numbers or morphologies on the molecule capture. Finally, we examine the details of the spatial patterns of molecule capture within the aesthetasc array. The cases and quantitative results are summarized in Table 1.

### 3.1. Flick outstroke versus return stroke

Odorant molecule fluxes to the aesthetasc surface during the flick outstroke and during the return stroke are shown in Figure 4a for the juvenile antennule and in Figure 4b for the adult antennule. In both cases the outstroke through an odor filament is characterized by a much steeper onset slope (i.e. rate of increase in molecule flux),
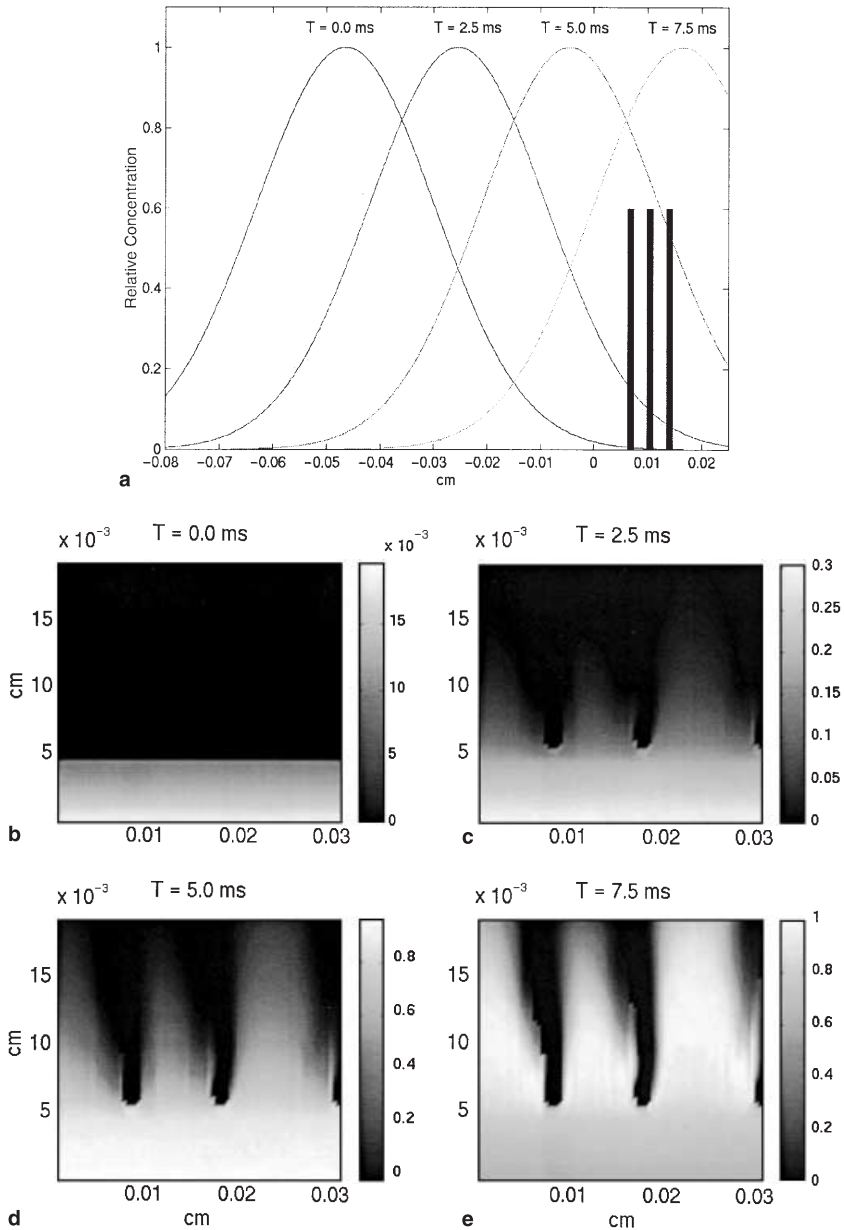
**Fig. 3.** Time development of odor filament moving through aesthetasc array; (a) Position of undisturbed Gaussian filament relative to aesthetascs at four times featured in Figs. (b)-(e), note that concentration is relative to the maximum of the initial filament, 100 mg/1; (b)-(e) Concentration field within the aesthetascs as antennule intersects odor filament, locations of aesthetascs are the same as in Fig. 1D.

**Table 1.** Features of molecule fluxes of the leading, distal aesthetasc for all runs discussed. Maximum flux is the peak of the molecule flux time series; Maximum onset slope is peak in the gradient of the flux time series; Total molecules is the integration of the molecule flux (and is per area).

| Morphology | Re | Outstroke or Return | Maximum Flux[1] | Maximum Onset Slope[2] | Total Molecules (per area)[3] |
|---|---|---|---|---|---|
| Adult | 1.68 | Out | 1.23E+12 | 3.76E+11 | 6.15E+12 |
| Adult | 0.84 | Return | 1.00E+11 | 1.44E+10 | 1.07E+12 |
| Adult | 0.27 | Out | 3.07E+09 | 1.41E+08 | 1.03E+11 |
| Adult | 0.13 | Return | 7.96E+07 | 1.77E+06 | 5.75E+09 |
| Adult | 0.13 | Out | 1.30E+08 | 2.93E+10 | 8.91E+09 |
| Adult | 0.065 | Return | 1.11E+08 | 1.24E+06 | 1.59E+10 |
| Juvenile | 1.68 | Out | 4.83E+13 | 2.98E+13 | 1.20E+14 |
| Juvenile | 0.84 | Return | 3.30E+12 | 1.01E+12 | 1.64E+13 |
| Juvenile | 0.27 | Out | 2.22E+11 | 2.16E+10 | 3.46E+12 |
| Juvenile | 0.13 | Return | 5.65E+09 | 2.61E+08 | 1.86E+11 |
| Juvenile | 0.13 | Out | 1.23E+10 | 5.73E+08 | 4.03E+11 |
| Juvenile | 0.065 | Return | 1.15E+09 | 2.67E+07 | 7.54E+10 |

[1]molecules/(ms $\mu^2$)
[2](molecules/(ms $\mu^2$)) / ms
[3]molecules/$\mu^2$

a much higher peak, and a shorter duration of odorant flux than during the slower return stroke through a filament of the same size and concentration distribution. These differences in molecule flux occur because the aesthetasc array is leakier to water flow and the velocity gradient along the surface of each aesthetasc is steeper during the rapid outstroke than during the slower return stroke.

Antennule speed, and thus aesthetasc $Re$, has a big effect on the flux of molecules to the surface of an aesthetasc (Table 1). The onset slope (Figure 5) and peak flux of molecules to the aesthetasc (Figure 6) increase with Re, both for antennules of juvenile morphology and of adult morphology. Furthermore, the total number of molecules encountered per area of an aesthetasc (i.e. the integrated molecule flux during a flick or during a return stroke) also increases with $Re$ (Figure 7), even though the duration of odorant flux to an aesthetasc is longer at lower $Re$. For stomatopods, whose aesthetascs are oriented at right angles to the oncoming flow during both the outstroke and the return stroke (Figure 1c,d), the differences in molecule flux between the outstroke and the return stroke are due primarily to the differences in speed (i.e. $Re$) between the rapid sweep out and the slower return. If the outstroke and return are conducted at the same $Re$, the onset slope, peak flux, and total molecules encountered per aesthetasc area are nearly the same during these two phases of the antennule flick (Table 1; Figures 5, 6, 7).

### 3.2. Juvenile versus adult

The fluxes of odorant molecules to the aesthetascs of juvenile and of adult stomatopods during the flick outstroke are shown in Figure 8a, and during the return stroke
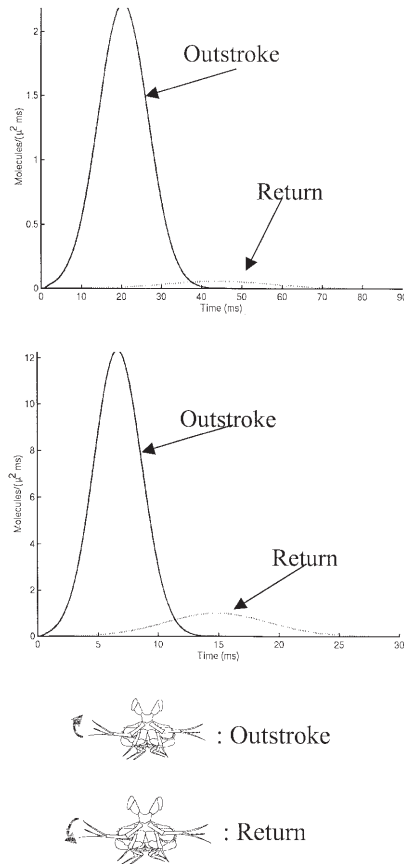
**Fig. 4.** Comparison of outstroke and return signals. Time series of molecule flux to the leading, distal aesthetasc during the outstroke and return stroke for (a) juvenile and (b) adult.

in Figure 8b. Both the onset slope and the peak are greater for the adult, whose aesthetascs operate at higher Re than do those of the juvenile. In contrast, juvenile aesthetascs encounter odor molecules for a longer time than do those of adults.

Not only do adult and juvenile aesthetascs operate at different Re, but their spatial arrangement on the antennule differs: the width of the gap between rows of aesthetascs relative to aesthetasc diameter is smaller in adults than in juveniles. If the antennules of stomatopods did not show this allometric growth, what would the consequences to molecule capture be during ontogeny? The aesthetascs of both juveniles and adults operate at a range of *Re* in which spacing between cylinders can have a large effect on leakiness of the array. If stomatopods were to maintain the juvenile morphology as they grow to adult *Re*, then the onset slope and peak of molecule flux to the aesthetascs would be much greater in adults than it is for the real adult morphology (Figure 9a). Conversely, if juvenile antennules operating at their lower *Re* were to have closely-spaced rows of aesthetascs like those on
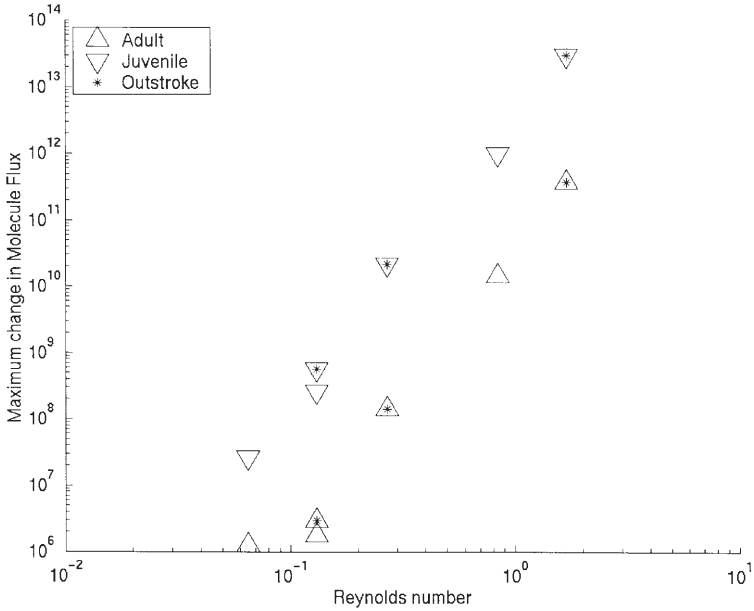
**Fig. 5.** Reynolds number dependence of the onset slope (maximum change in molecule flux to the leading, distal aesthetasc) for all runs described in Table 1. Adults are denoted by circles, juveniles by triangles. Outstrokes are indicated by the large asterisk inside the symbol (open symbols are return strokes).

adults, then the flux of molecules to the aesthetascs would be very low (Figure 9b). Across the range of $Re$ we tested, the juvenile morphology (with widely-spaced rows of aesthetascs) results in steeper onset slopes, higher peak fluxes, and greater numbers of molecules captured during a flick, than does the adult morphology (with closely-spaced rows of aesthetascs) operating at the same aesthetasc $Re$ (Table 1; Figures 5, 6, 7).

### 3.3. Proximal versus distal ends of an aesthetasc

Because our sampling plane intersects antennules at different distances from their attachment to the antennule (Figure 1c), we can compare the flux of molecules to the distal versus proximal regions of an aesthetasc. The onset slope, peak flux, and total number of molecules encountered per area of an aesthetasc during a flick outstroke are greater at the distal portion of an aesthetasc that at its proximal region, both for juveniles (Figure 10a) and adults (Figure 10b). The lower flux to the proximal region is due to the boundary layer that has developed along the surface of the antennule to which the aesthetasc is attached. Since the $Re$ of the adult antennule is higher than that of the juvenile antennule, the boundary layer along an adult antennule is thinner relative to aesthetasc length than it is in the juvenile [49], [54]. Therefore, the relative difference in flux between the middle of the proximal
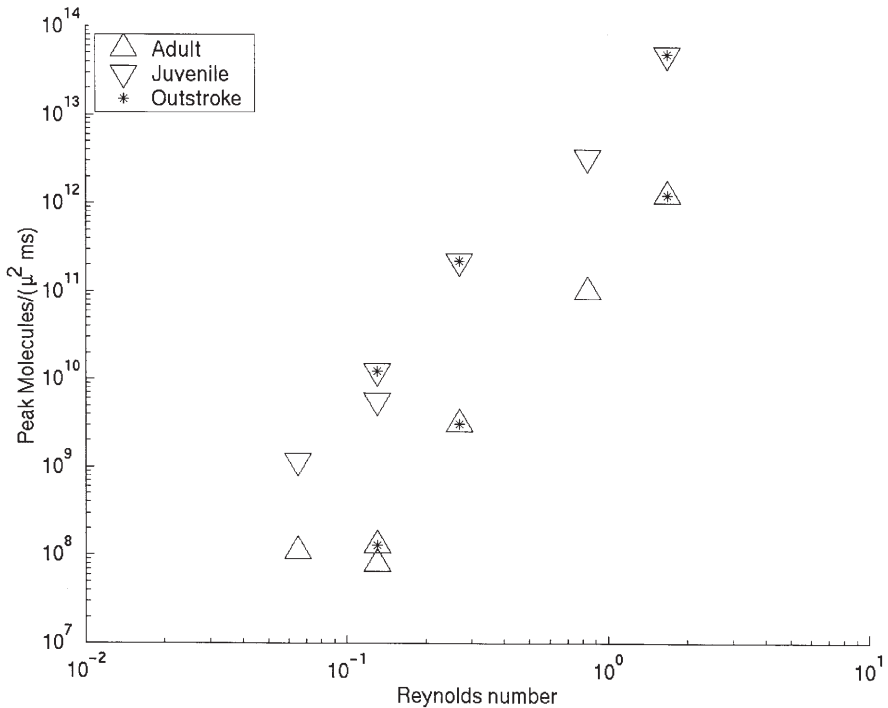
**Fig. 6.** Reynolds number dependence of the maximum molecule flux to the leading, distal aesthetasc for all runs described in Table 1. Adults are denoted by circles, juveniles by triangles. Outstrokes are indicated by the large asterisk inside the symbol (open symbols are return strokes).

half of an aesthetasc and the middle of the distal half is smaller for the adult than for the juvenile.

### 3.4. Aesthetasc position in a row

The aesthetascs on a stomatopod antennule are arranged in rows, with three aesthetascs per row (Figure 1a). The rows are parallel to the direction of water flow relative to the antennule during the flick outstroke and return. Therefore, the middle and trailing aesthetascs in a row are directly downstream from the leading aesthetasc (Figure 1c). During the outstroke, peak molecule flux to the downstream aesthetasc in a row is only about one seventh of peak flux to the upstream aesthetasc in the row, for both juveniles (Figure 11a) and adults (Figure 8b). This effect is due to the removal of molecules from the odor filament by the upstream and middle aesthetascs before the filament reaches the downstream aesthetasc, and to the shearing and diffusion of the odor filament during the time it is carried past the aesthetascs (Figure 3). The signal arrives later to the downstream aesthetasc, and the onset slope and total number of molecules per area captured is also lower for the downstream than for the upstream aesthetasc.
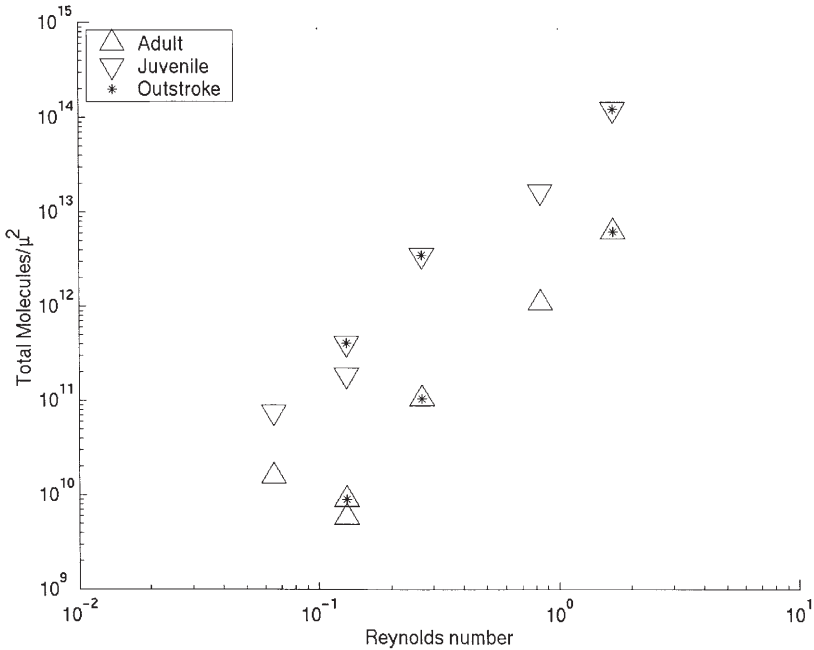
**Fig. 7.** Reynolds number dependence of the total molecule flux to the leading, distal aesthetasc for all runs described in Table 1. Adults are denonted by circles, juveniles by triangles. Outstrokes are indicated by the large asterisk inside the symbol (open symbols are return strokes).

The ratio of molecule flux to the downstream aesthetasc in a row to molecule flux to the upstream aesthetasc provides an index of how easily odors can move into the array of aesthetascs by advection and molecular diffusion (Table 2). The higher this "accessibility ratio", the more readily molecules can penetrate into the array of aesthetascs. If we compare an antennule with adult morphology (with closely-spaced rows of aesthetascs) to one with juvenile morphology (with widely-spaced rows) operating at the same Re, the accessibility ratio is much greater for the juvenile (Table 2). However, because the larger adult antennules flick at higher Re than juvenile antennules, the accessibility ratio of the array of aesthetascs on an antennule does not change as the stomatopods grow (Table 2).

## 4. Discussion

We have developed a model of molecule flux to the surface of chemosensory hairs (sensilla) on olfactory antennae of arthropods, and have applied the model to the case of odorant capture by the aesthetascs on flicking antennules of mantis shrimp. While earlier advection-diffusion models of odorant capture by antennae have focused on an isolated sensillum, we have developed a model that incorporates velocity vector fields measured for complex three-dimensional arrays of hairs on antennae. These measured velocity fields are analyzed in a two-step process to define the optimal
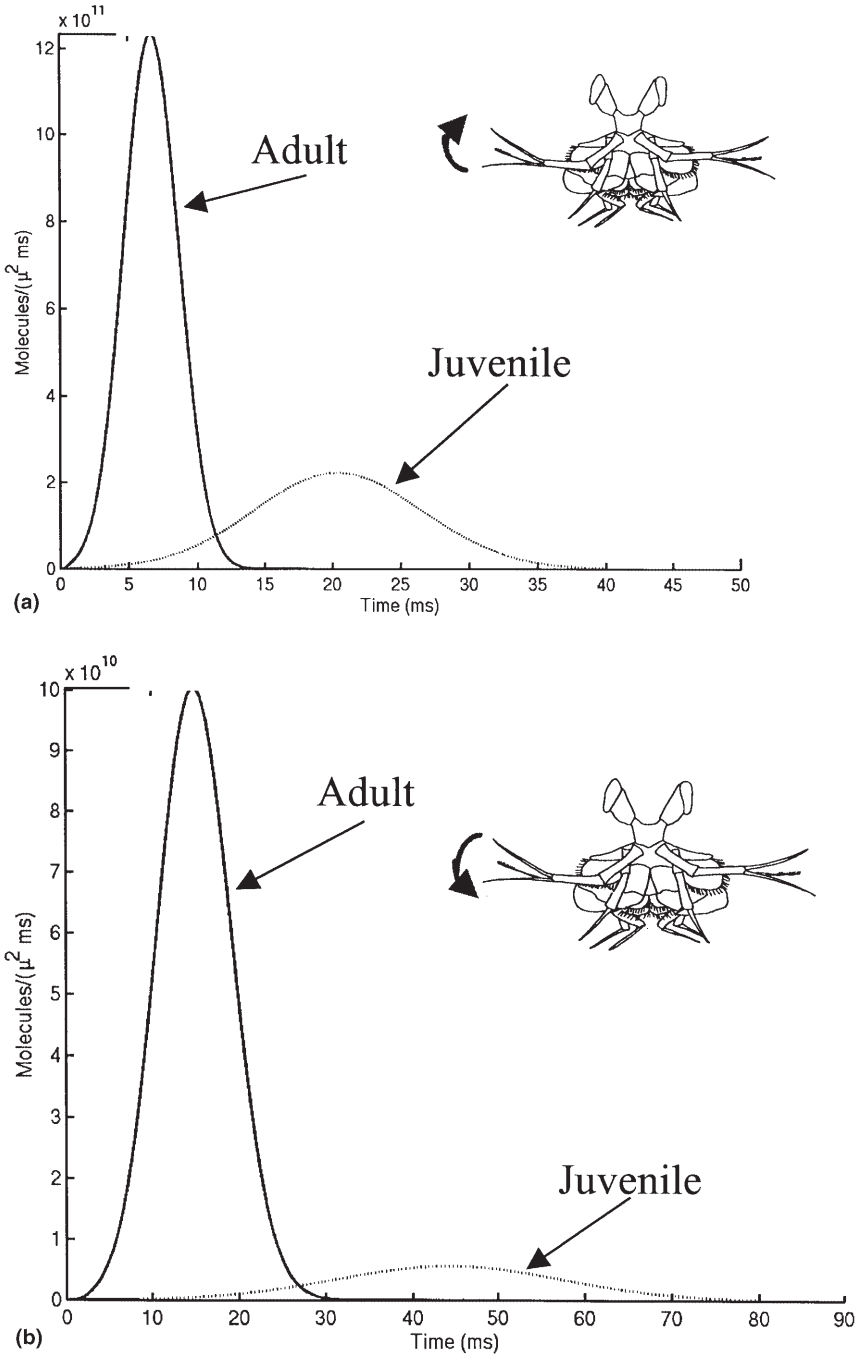
**Fig. 8.** Comparison of adult and juvenile individuals. Time series of molecule flux to the leading, distal aesthetasc for the adult and the juvenile individual during (a) the outstroke and (b) the return stroke.
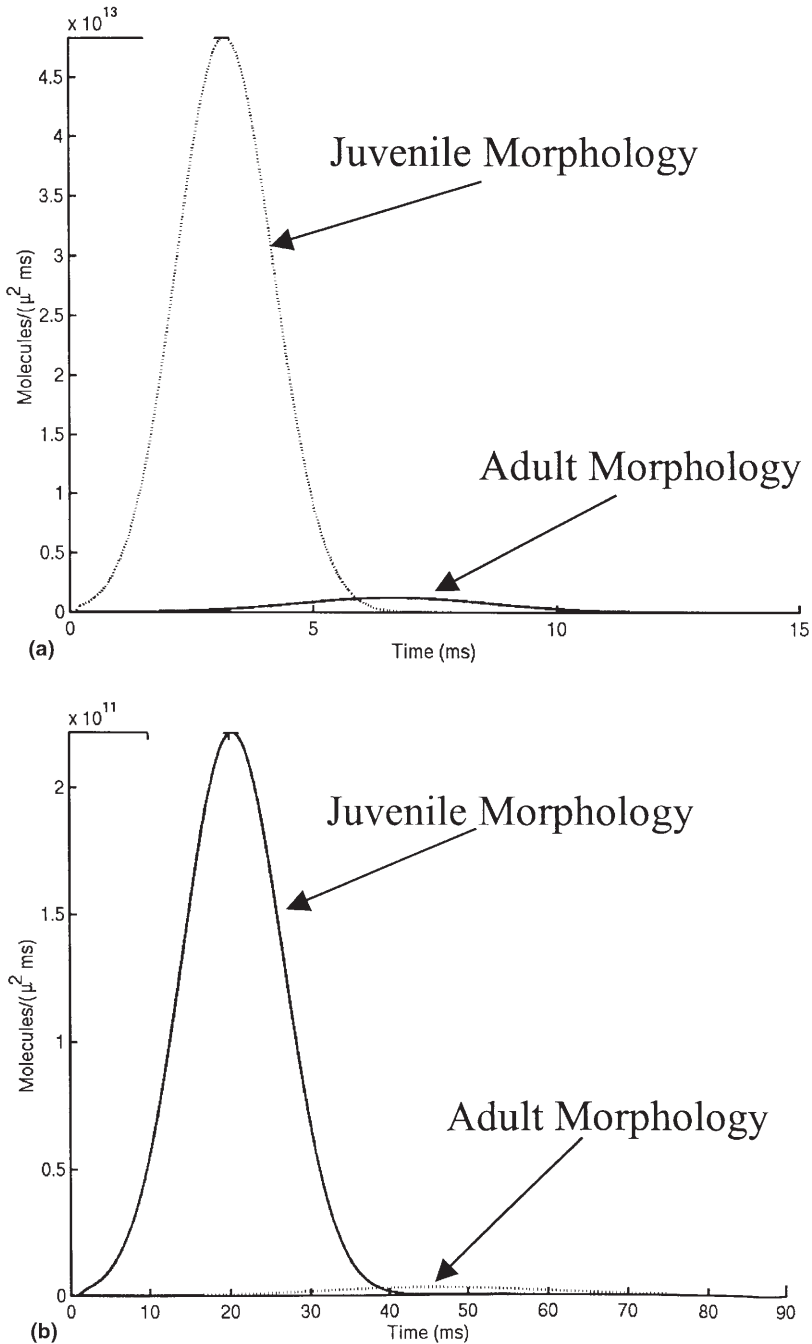
**Fig. 9.** Effects of morphology. Time series of molecule flux to the leading, distal aesthetasc for the adult and juvenile morphologies (i.e., gap-to-diameter ratio) during the outstroke at (a) the adult Reynolds number (1.68) and (b) the juvenile Reynolds number (0.27).
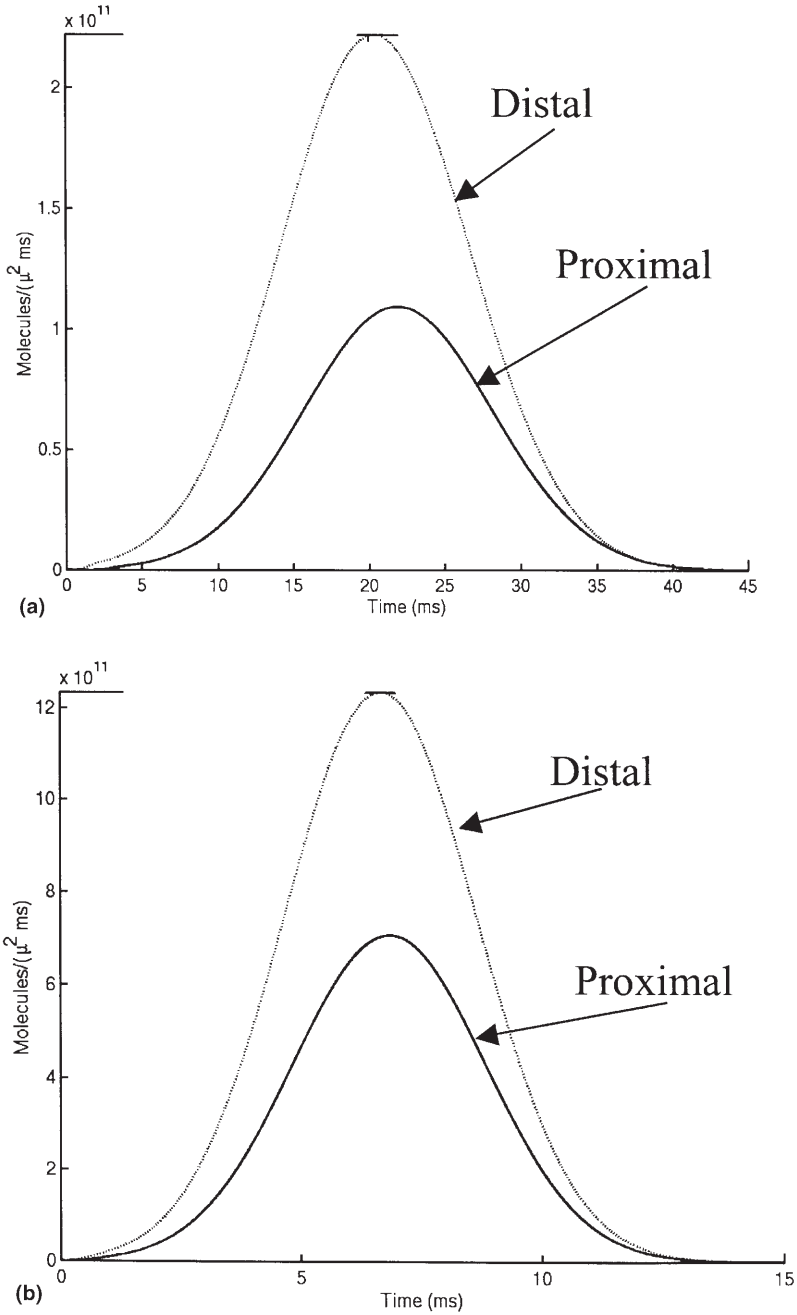
**Fig. 10.** Proximal versus distal signal. Time series of molecule flux to the leading proximal and distal aesthetascs during the outstroke for the (a) juvenile and (b) adult.

**Table 2.** Comparison of molecule fluxes to the leading and trailing distal aesthetascs during the outstroke. Accessibility index is defined as the ratio of the flux to the trailing aesthetasc to the flux to the leading aesthetasc and is related to the leakiness of the aesthetasc array.

| | Re | Maximum Flux, Leading Aesthetasc[1] | Maximum Flux, Trailing Aesthetasc[1] | Accessibility Index, Trailing:Leading Ratio |
|---|---|---|---|---|
| Adult | 1.68 | 1.23E+12 | 1.66E+11 | 1.35E-01 |
| Juvenile | 0.27 | 2.22E+11 | 3.13E+10 | 1.41E-01 |
| Adult | 0.27 | 3.07E+09 | 6.84E+07 | 2.23E-02 |
| Adult | 0.13 | 1.30E+08 | 1.27E+07 | 9.73E-02 |
| Juvenile | 1.68 | 4.83E+13 | 8.24E+12 | 1.71E-01 |
| Juvenile | 0.13 | 1.23E+10 | 1.18E+09 | 9.55E-02 |

[1]molecules/(ms $\mu^2$)

flow field for use with the numerical model: (1) an initial estimate of the velocity field is made by decomposing the observed flow-field into a divergent portion and a non-divergent portion; and (2) the optimal velocity field is defined by adjusting this velocity field to minimize the mean-square-error of the model field (as compared to the measured field) while applying the strong constraint that the flow field obey the continuity equation.

Incorporating flow fields through arrays of sensilla is important because, in a critical Reynolds number range that depends on hair spacing, a transition occurs in the proportion of the fluid encountering a hair array that flows through the array rather than around it (the "leakiness"). Our modeling approach, applied to stomatopod sensilla (aesthetascs), permitted us to quantify the large increases in biologically-important aspects of the molecule flux to chemosensory hairs that occur when antennule velocity is increased in the *Re* range in which the transition to higher leakiness occurs. This transition is characterized by: steepened onset slope of molecule flux, increased total number of molecules captured during an antennule stroke through an odor filament, and elevated accessibility of aesthetascs in the middle and back of the array to diffusing molecules.

In contrast to previous experimental studies, which showed that pulses of water flow enhance odorant penetration into aesthetasc arrays [70], [66], [3], [58], [60], [32], our model enables us to quantify molecule flux to aesthetasc surfaces when the small-scale velocity field around aesthetascs actually mimics that during antennule flicking and when the spatial distribution of odorant concentration in the water mimics that in turbulent odor plumes.

## 4.1. Sniffing

Many types of animals enhance the flux of odorant molecules from the ambient water or air to the surfaces of their olfactory organs by moving the fluid across or through them [24], [52]. Our results corroborate earlier suggestions that antennule flicking by crustacean antennules also serves this function [70], [66], [3], [58], [60], [32], [55].

The olfactory sensilla (aesthetascs) on stomatopod antennules operate in a *Re* range in which the speed at which they move through the surrounding fluid can have very a large effect on the leakiness of the array to fluid flow [17], [18], [43], [44], [46], [48], [47]. Our calculations of the diffusion of molecules from odor filaments to the surfaces of stomatopod aesthetascs demonstrate that increases in the leakiness to fluid flow through an array of aesthetascs result in increases in the flux of molecules to the surfaces of those aesthetascs.

When stomatopods flick their antennules, the outstroke is faster than the return stroke. This difference in velocity occurs in a *Re* range in which velocity has a big effect on the leakiness of arrays of sensilla with spacings like those of the rows of aesthetascs on stomatopod antennules. Therefore, the result of the asymmetry in velocity during a flick is that more water passes through the array of aesthetascs during the outstroke than during the return. One consequence of this difference in leakiness is that the array of sensilla on an antennule do not end up surrounded by the same water in which they started before the flick; rather, they flush out "old" water from between the aesthetascs and pick up new water during the outstroke when the array is leaky, and then retain that water between the aesthetascs during the return stroke and during the pause before the next flick [48]; [47]; [34]; [55].

The results of the simulations presented in this study reveal another consequence of the difference in leakiness between the flick outstroke and return: the flux of molecules to the aesthetascs during the outstroke is much greater than during the return stroke. Even if an antennule encounters an odor filament during the return stroke, the peak molecule flux to the aesthetascs, the onset slope of molecule flux, and total number of molecules captured per area of aesthetasc is much lower than it would be if that odor filament were encountered during the outstroke.

The increased leakiness and the increased odor "accessibility index" during the flick outstroke suggest that stomatopods can take discrete odor samples in space and time. Each flick outstroke acts in a manner analogous to a sniff. The results of our flow measurements [55] and molecule flux calculations (this study) are consistent with earlier studies that also suggested that flicking permits increased odor access to the aesthetascs [66], [3], [70], [58], [60], [32]. However, our study also points out the importance of the flow-field asymmetries (due to the change in Reynolds number) in the flick outstroke versus return stroke in permitting the antennule to take discrete odor samples, i.e. to sniff.

### 4.2. *Growth and scaling of antennules during ontogeny*

The olfactory hairs (aesthetascs) on stomatopod antennules operate in a *Re* range in which the size of the gap between closely-spaced aesthetascs can have big effect on the leakiness of the array, and in which the array is most sensitive to velocity changes [17], [18], [43], [44], [46], [48], [47]. As stomatopods grow, the *Re* of their aesthetascs increases. However, the geometry of a stomatopod's antennules also changes as the animal becomes bigger: the width of the gap between rows of aesthetascs becomes narrower relative to the diameter of the aesthetascs as stomatopods grow. One consequence of this allometric growth is that the asymmetry in the leakiness of the aesthetasc array between the outstroke and the return stroke is
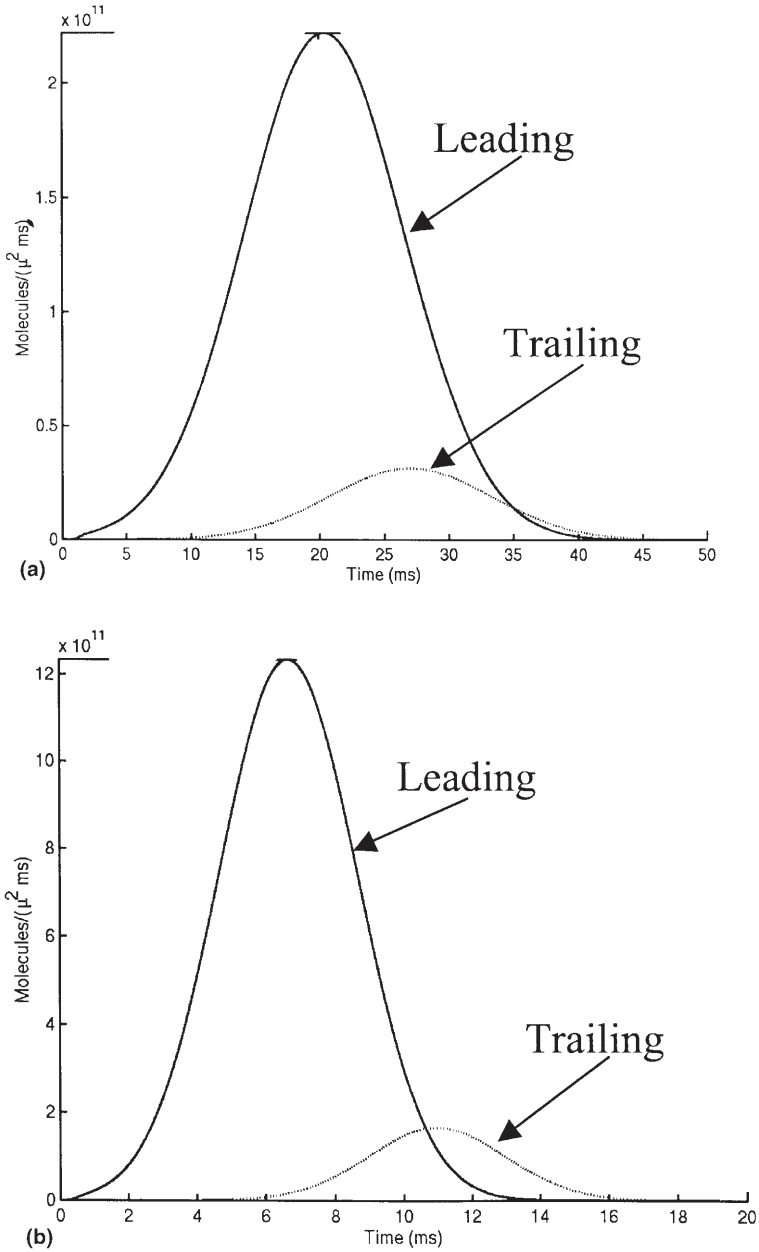
**Fig. 11.** Effects of aesthetasc position in a row. Time series of molecule flux to the leading and trailing distal aesthetascs during the outstroke for (a) juvenile and (b) adult.

maximized at each antennule size [55]. Furthermore, the odor "accessibility index" of the aesthetasc array is maintained as the antennules grow ("accessibility index" is the ratio of molecule flux at the downstream aesthetasc in a row to molecule flux at the upstream aesthetasc, an index of how easily odors can move into the array of aesthetascs, Table 2).

Another consequence of the allometric growth of stomatopod antennules is that the flux of molecules to the surfaces of the aesthetascs during the flick does not increase as drastically with growth as it would if aesthetasc gap-to-diameter ratios were maintained as the animals grow (i.e., if they showed geometric, rather than allometric, growth). In fact, our calculations show that the total number of molecules captured by an antennule during a flick through an odor filament would be slightly *more* if they grew geometrically than it is for the actual, allometric growth (figure 12), even though the antennule contains fewer aesthetascs under the assumption of geometric growth. However, we note that the allometric growth shown by stomatopods also results in a longer antennule (more segments). This extension of the antennule increases the range of fluid sampled by each flick and makes it more likely that a filament of odor is encountered, which may compensate to some extent for the reduction in molecules captured per filament. In addition, behavioral changes, including more frequent flicking (by more than a factor of 2, [54]), may further compensate for this reduction in molecules captured per filament. Nonetheless, the fact that stomatopods maintain the asymmetry in flow leakiness and molecule accessibility between the antennule outstroke and return stroke as they grow, even though the total molecule flux is reduced by the reduction in the gap-to-diameter ratio which occurs during allometric growth, suggests that the ability to take discrete odor samples in space and time is important to stomatopod olfaction.

*4.3. Design of hair-bearing olfactory antennae*

Like stomatopods, other malacostracan crustaceans, such as lobsters and crabs, have odor-capturing antennules that bear arrays of hair-like chemosensory aesthetascs. When stomatopods [54], lobsters, and crabs [48], [47] flick their antennules, their aesthetascs operate in a range of *Re* in which changes in velocity and changes in aesthetasc spacing can have large effects on the leakiness of the array of aesthetascs. The study presented here shows that such changes in leakiness can have large effects on the performance of the aesthetascs in capturing molecules from the surrounding fluid. Thus, differences between the velocity or aesthetasc spacing during the flick outstroke and return stroke in this critical *Re* range can permit the antennules to take discrete odor samples in space and time, i.e. to sniff.

Like stomatopods, spiny lobsters sniff by moving their antennules more rapidly during the flick downstroke than during the return stroke [48], [47]. Flume studies using planar laser induced fluorescence to quantify concentrations encountered by aesthetasc arrays on lobster antennules flicking in turbulent dye plumes showed that, even in ambient water currents, dye does not penetrate into the array of aesthetascs except during the flick downstroke (Koehl, Koseff, Crimaldi, McCay, Cooper, and Wiley, in prep.). (This difference in water penetration is due to the direction of the flow relative to the antennule: flow due to the flick is at right angles to the antenn-
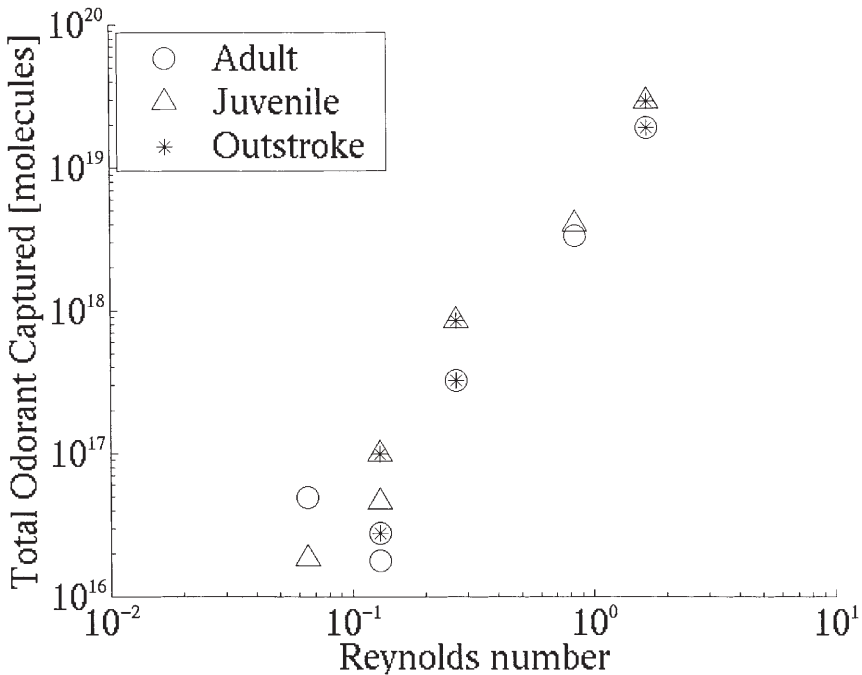
**Fig. 12.** Total odorant captured during an encounter with a single filament. Calculation of total odorant captured based on the integrated molecule flux (Fig. 7) multiplied by total area of sensillar surface for the adult and juvenile models. Assumed dimensions: aesthetasc diameter = 10 μ for juveniles, 20 μ for adults; aesthetasc length = 325 μ for juvenile, 516 μ for adults; number of aesthetascs = 12 for juveniles, 48 for adults.

ule, whereas flow due to ambient currents when an animal is moving upstream, as lobsters do when tracking an odor plume, is parallel to the length of the antennule.) While stomatopods maintain their ability to sniff as they grow by changes in the spacing of the aesthetascs on the antennule, lobsters do so by maintaining the *Re* of their aesthetascs as they grow [12]; [34].

In contrast to stomatopods and lobsters, which have rows of aesthetascs spaced along long antennules, crabs have aesthetascs that are arranged in a tightly packed bunch (like the bristles on a toothbrush) at the end of short antennules. When crabs flick their antennules, the aesthetascs are passively splayed apart during the flick outstroke, but are pushed back together during the return stroke. This particular change in the spacing of the aesthetascs of blue crabs has an enormous effect on water penetration into the aesthetasc array at the *Re* at which they operate during a crab flick [48], [47].

The diverse examples of crustacean olfactory antennules described above illustrate that no particular hair arrangement optimizes the ability to sniff. Species or life stages with different hair sizes and spacings can alter the leakiness of their antennules by flicking in the *Re* range at which the leakiness of their particular hair

array is especially sensitive to changes in velocity or hair spacing. Therefore, by altering the fluid velocity encountered by an olfactory appendage or by changing the aesthetasc spacing, the animals can change the flux of molecules to the surfaces of their chemosensory aesthetascs. By operating in this critical $Re$ range, these antennules can sniff.

## 5. Conclusions for stomatopod antennules

The use of numerical simulation of odorant transport into and through an array of aesthetascs allows us to examine the details of the signal actually detected by a marine species in an odor plume. Because the flick of a stomatopod antennule consists of an asymmetric outstroke and return stroke, the individual is able to take discrete samples of odorant, analogous to sniffing. The leakiness of the aesthetasc array during the rapid outstroke permits much greater odorant penetration of the aesthetasc array, leading to higher peak fluxes at the aesthetascs, greater onset slope and more total molecules detected than during the return stroke. The ability of the odorant to penetrate into the aesthetasc array has been captured quantitatively through the accessibility index, which is the ratio of the peak flux at the leading aesthetasc to the peak flux at the trailing aesthetasc, a quantity expected to be related to the leakiness of the array.

As stomatopods grow and their $Re$ increases, the rows of aesthetascs on the antennules become more closely-spaced relative to aesthetasc diameter. This allometric growth maintains the ability to sniff (i.e. the asymmetry in leakiness and molecule flux between the outstroke and return stroke) and maintains the accessibilty of diffusing molecules to aesthetascs within the array during the ontogeny of stomatopods. In fact, the numerical simulations indicate that the accessibility index and leakiness are preserved as the individual matures, suggesting that they may be an important factors in the ability of an individual to detect odors in its environment.

## References

1. Ache, B.W.: *The Biology of the Crustacea, Vol. 3* (Academic Press, New York 1982) 369–393
2. Adam, G., Delbruck, M.: *Structural Chemistry and Molecular Biology* (Freeman and Co., San Francisco 1968) 198–215
3. Atema, J.: Society of Experimental Biology Symposium, **39**, 3887–3423 (1985)
4. Atema, J.: *Chemical Ecology: The Chemistry of Biotic Interaction* (National Academy Press, Washington DC 1995) 147–159
5. Atema, J.: Biol. Bull., **191**, 129–138 (1996)
6. Atema, J., Moore, P. A., et al.: Mar. Ecol. Prog. Ser., **74**, 303–306 (1991)
7. Atema, J., Voigt, R.: *Biology of the Lobster Homarus americanus* (Academic Press, San Diego, CA 1995) 313–348
8. Barlow, D.J.: Physiol. Lond., **141**, 337–350 (1958)

9. Berg, H.C., Purcell, E.M.: Biophysical Journal, **20**, 193–219 (1977)
10. Berg, H. C.: *Random Walks in Biology* (Princeton University Press, Princeton, NJ 1983)
11. Berg, K., Voigt, R., et al.: Biological Bulletin, **183**, 377–378 (1992)
12. Best, B.A.: Am. Zool., **35**, 53A (1995)
13. Boeckh, J., Kaissling, K.E., et al.: Cold Spring Harbor Symp. Quant. Biol., **30**, 263–280 (1965)
14. Caldwell, R.L.: Animal Behavior, **27**, 194–201 (1979)
15. Caldwell, R.L.: Mar. Behav. Physiol., **8**, 189–197 (1982)
16. Caldwell, R.L.: Animal Behavior, **33**, 101–106 (1985)
17. Cheer, A.Y.L., Koehl, M.A.R., I.M.A.: J. Math. Appl. Med. Biol., **4**, 185–199 (1987)
18. Cheer, A.Y.L., Koehl, M.A.R.: Journal of Theoretical Biology., **129**, 17–39 (1987)
19. Cowen, E.A., Monismith, S.G.: Experiments in Fluids, **22**, 199–211 (1997)
20. Crimaldi, J., Koseff, J.: Experiments in Fluids (2001, in press)
21. *CRC Handbook of chemistry and physics*, Lide, D.R., ed., (CRC Press, Boca Raton, FL 1991)
22. DeSimone, J.A.: *Biochemistry of Taste and Olfaction*, Cagen, R.H., Kare, M.R., eds. (Academic Press, N.Y. 1981) 213–229
23. Devine, D.V., Atema, J.: Biol. Bull., **163**, 144–153 (1982)
24. Doving, K.B., Dubois-Dauphin, M. et al.: Acta Zool. **58**, 245–255 (1977)
25. Elkington, J.S., Carde, R.T.: *Chemical Ecology of Insects,* Bell, W.J., Carde, R.T. eds., (Elsevier Press, Amsterdam 1984) 73–91
26. Ferziger, J.H., Peric, M.: *Computational methods for fluid dynamics*, (Springer-Verlag, New York 1996)
27. Finelli, C.M., Pentcheff, N.D. et al.: Limnology and Oceanography, **44**, 1056–1071 (1999)
28. Futrelle, R.P.: Trans. Neurosci., **4**, 116–120 (1984)
29. Getchell, T.V., Getchell, M.L.: Chem. Senses, **2**, 313–326 (1977)
30. Getchell, T.V., Margolis, F.L., et al.: Prog. Neurobiol., **23**, 317–345 (1984)
31. Gleeson, R.A.: Biological Bulletin, **163**, 162–171 (1982)
32. Gleeson, R.A., Carr, W.E.S., et al.: Chemical Senses, **18**, 67–75 (1993)
33. Gleeson, R.A., McDowell, L.M. et al.: Cell Tissue Research, **284**, 279–288 (1996)
34. Goldman, J.A., Koehl, M.A.R.: Chem. Senses, (2001, in press)
35. Gomez, G., Atema, J.: J. Exp. Biol., **199**, 1771–1779 (1996)
36. Hadfield, M.G., Scheuer, D.: Bulletin of Marine Science, **37**, 556–566 (1985)
37. Hallberg, E., Johansson, K.U.I., et al.: Microscopy Research and Technique, **22**, 325–335 (1985)
38. Hallberg, E., Johansson, K.U.I., et al.: Int. J. Insect Morph. Embryol., **26**, 173–180 (1997)
39. Happel, J., Brenner, H.: *Low Reynolds Number Hydrodynamics* (Prentice-Hall, Englewood Cliffs, New York 1965)
40. Heimann, P.: Cell Tissue Research, **235**, 117–128 (1984)
41. Hood, Grover, Science, **184**, 1003–1005 (1974)
42. Kaissling, K.E.: *Biochemistry of Sensory Functions* (Springer-Verlag, Berlin 1987) 243–273
43. Koehl, M.A.R.: Contemporary Mathematics, **141**, 33–64 (1993)
44. Koehl, M.A.R.: Soc. Exp. Biol. Symp. **49**, 157–182 (1995)
45. Koehl, M.A.R.: Mar. Fresh. Behav. Physiol., **27**, 127–141 (1996)
46. Koehl, M.A.R.: Oceanography, **11**, 10–12 (1998)
47. Koehl, M.A.R.: Conference proceeings of the IMA Workshop on Computational Modeling in Biological Fluid Dynamics (2000, in press)

48. Koehl, M.A.R.: Math. Meth. Appl. Sci., **24**, (2001, in press)
49. Kundu, P.K.: *Fluid Mechanics*, (Academic Press, San Diego, CA 1990)
50. Leonard, B.: J. Num. Meth. Fluids, **16**, 200–220 (1991)
51. Loudon, C., Best, B.A., et al.: Journal of Experimental Biology, **193**, 233–254 (1994)
52. Loudon, C., Koehl, M.A.R.: J. Exp. Biol., **203**, 2977–2990 (2000)
53. Mankin, R.W., Mayer, M.S.: Experientia, **40**, 1251–1252 (1984)
54. Mead, K.S., Koehl, M.A.R., et al.: J. Exp. Mar. Biol. Ecol., **241**, 235–261 (1999)
55. Mead, K.S., Koehl, M.A.R.: J Exp. Biol. **205**, 3795–3808 (2000)
56. Mellon, J., D.F., Alones, V.E.: Micros. Res. Tech., **24**, 231–259 (1993)
57. Mellon, J., D.F., Alones, V.E.: J. Comp. Physiol. A., **181**, 205–216 (1997)
58. Moore, P.A., Gerhardt, G.A., et al.: Chemical Senses, **14**, 829–840 (1989)
59. Moore, P.A., Atema, J.: Biol. Bull., **181**, 408–418 (1991)
60. Moore, P.A., Atema, J., et al.: Chemical Senses, **16**, 663–674 (1991)
61. Moore, P.A., Scholz, N., et al.: Journal of Chemical Ecology, **17**, 1293–1307 (1991)
62. Moore, P.A.: Chemical Senses, **19**, 71–86 (1994)
63. Murlis, J.: *Mechanism of Insect Olfaction,* Payne, T.L., ed., (Clarendon Press, NJ 1986) 27–38
64. Murray, J.D.: *Nonlinear differential equation models in biology* (Oxford Univ. Press, Oxford 1977) 83–127
65. Nachbar, R.B., Morton, T.H.: J. Theor. Biol., **84**, 387–407 (1981)
66. Schmidt, B.C., Ache, B.W.: Science, **205**, 204–206 (1979)
67. Schmidt, M., Ache, B.W.: Journal of Comparative Physiology A, **178**, 605–628 (1996)
68. Schneider, R.W.S., Price, B.A. et al.: J. Insect Physiol., **44**, 677–684 (1998)
69. Schneider, R.W.S., Lanzen, J., et al.: J. Comp. Phys., **182**, 287–298 (1998)
70. Snow, P.J.: J. Exp. Biol., **58**, 745–766 (1973)
71. Vogel, S.: *Life in Moving Fluids* (Princeton University Press, Princeton, NJ 1994)
72. Webster, D.R., Rahman, S., Dasi, L.P.: Limnol. Oceanogr. (2001, in press)
73. Weissburg, M.J., Zimmer-Faust, R.K.: Ecology, **74**, 1428–1443 (1993)
74. Weissburg, M.J., Zimmer-Faust, R.K.: J. Experimental Biology, **197**, 349–375 (1994)
75. Weissburg, M.J.: J. Comparative Physiology A, **85**, 229–238 (1999)
76. Weissburg, M.J.: Biol. Bull., **198**, 188–202
77. Zimmer-Faust, R.K.: Limnology and Oceanography, **34**, 1364–1374 (1989)
78. Zimmer-Faust, R.K.: Biological Bulletin, **181**, 419–426 (1991)
79. Zimmer-Faust, R.K., Finelli, M., et al.: Biol. Bull., **188**, 111–116 (1995)